Crystal Structures and Physicochemical Properties of Be_2N and Mg_2N as Electride Materials

Gui Wang,[1,2] Zhuang Ma,[1,2] Jing-Wen Jiang,[1,2] Jing-kai Yang,[3] Yi-Ling Sun,[1,2] Zheng-Fang Qian,[1,2] Pu Huang,[1,2] Peng Zhang,[1,2,*,†] and Su-Huai Wei[4]

[1] *College of Physics and Optoelectronic Engineering, Shenzhen University, Shenzhen 518060, China*

[2] *Key Laboratory of Optoelectronic Devices and Systems of Ministry of Education and Guangdong Province, College of Physics and Optoelectronic Engineering, Shenzhen University, Shenzhen 518060, China*

[3] *Hebei Key Laboratory of Applied Chemistry, College of Environmental and Chemical Engineering, Yanshan University, Qinhuangdao 066004, China*

[4] *Beijing Advanced Innovation Center for Materials Genome Engineering, Beijing Computational Science Research Center, Beijing 100193, China*

(Received 27 July 2022; revised 19 October 2022; accepted 9 February 2023; published 3 March 2023)

Electrides are a special family of materials with exotic physical properties and various crystal structures in different dimensions. Among them, alkaline-earth metal nitrides (AE_2N) have attracted enormous attention, since the synthesis of Ca_2N as a two-dimensional (2D) electride. However, apart from Ca_2N, the physicochemical properties of other AE_2N are not well understood, and in some cases, their crystal structures remain unknown. To overcome these issues, here, we conduct systematic investigations into the crystal structures, electronic structures, and optical properties of two typical AE_2N, i.e., Mg_2N and Be_2N, based on first-principles calculations. By symmetry analysis, we derive a crystal structure with $R\bar{3}m$ symmetry for Be_2N, which is energetically more stable than all the other structures proposed previously. Our calculations show that $R\bar{3}m$ Be_2N is a 2D electride with the anionic electrons located in the interstitial space, forming a 2D Kagome lattice. Moreover, distinct from traditional 2D electrides, it exhibits anomalous physicochemical properties, such as having a small interstitial space, a high work function, and a large cleavage energy, mainly due to the relatively strong bonding effect between anionic electrons and cationic framework. For Mg_2N, on the other hand, we find that the most stable structure has $R3m$ symmetry, which shows a total energy of 0.005 eV per formula unit lower than the previously predicted $Cmcm$ structure. Moreover, different from $R\bar{3}m$ Be_2N, $R3m$ Mg_2N is identified as a zero-dimensional (0D) electride with a semiconducting band structure, since its anionic electrons are confined in separated 0D cavities and cannot interact with each other. These studies thus provide a deeper understanding of the crystal structures and physicochemical properties of Be_2N and Mg_2N as potential electride materials.

DOI: 10.1103/PhysRevApplied.19.034014

I. INTRODUCTION

Electrides constitute an emerging class of materials constructed by a cationic framework with excess electrons located in their structural cavities, which serve as anions [1]. In these materials, the anionic electrons are not bound to any nucleus, and thus, are usually free to diffuse and easy to extract, which lead to exotic physical properties, such as high electrical conductivities and low work functions (W_F). These fascinating properties have a major fillip for various technologies, including superconductors [2,3], transparent conductors [4], high-harmonic generation [5], ferromagnets [6], electrodes [7], light-emitting diodes (LEDs) [8], ammonia synthesis [9], and CO_2 splitting [10], which have spurred tremendous research interest in electrides over the past 30 years.

Historically, the electride, $Cs^+(15\text{-crown-}5)2\cdot e^-$, was realized in an organic crystal by Dye and co-workers in 1982 [11,12]. After that, a series of organic compounds were synthesized and identified as electrides [13–16]. However, most of these organic electrides are rather unstable and sensitive to heat and O_2/water, such that their intrinsic properties remained almost undetermined [17]. The situation did not change until 2003, when the inorganic electride, $[Ca_{24}Al_{28}O_{64}]^{4+}(e^-)_4$, was successfully synthesized by Matsuishi *et al.* [18], which possessed a good thermal stability at room temperature [4,19,20].

*pzhang_xmu@foxmail.com
†pengzhang@szu.edu.cn

Since then, a variety of stable inorganic electrides have been found experimentally, including Ca_2N [21], LaRuSi [22], Sr_5P_3 [23], $Ti_2(O/S)$ [24], and Hf_2S [25], with their physicochemical properties carefully studied. In addition, with the development of computational techniques, hundreds of potential electrides were also recently predicted by density-functional-theory- (DFT) based high-throughput calculations, which significantly expand the boundary of the electride family [26–30].

Generally speaking, according to the connectivity of cavities and channels in their crystal structures, electrides can be classified into four categories: zero- (0D), one- (1D), two- (2D), and three-dimensional (3D) electrides [31,32]. Among them, 2D electrides are a class of materials with the anionic electrons confined in a 2D space sandwiched by adjacent cationic slabs, with Ca_2N as the prototype material. It is interesting to see that Ca_2N can achieve an electron mobility of 520 $cm^2\,V^{-1}\,s^{-1}$ at 2 K, along with a mean scattering time of 0.6 ps and a mean free path of 0.12 μm, which together results in a rather high electrical conductivity, even higher than that of metal Ca [21]. Moreover, distinct anisotropy in electron transport and magnetic resistance are also observed in Ca_2N [33]. These interesting properties make Ca_2N a promising candidate for various electronic applications, and thus, encourages plenty of efforts to explore 2D electrides, such as other alkaline-earth metal nitrides, AE_2N (AE = Be, Mg, Ca, Sr, Ba). Among them, Sr_2N and Ba_2N are found to have the same crystal structure as Ca_2N [34,35], but with poor stability under oxygen and/or moisture conditions [35]. While, on the other hand, Be_2N and Mg_2N have not been experimentally synthesized. Based on the *ab initio* crystal-structure-search method, Ma and co-workers [31] reported that Be_2N and Mg_2N might have trigonal ($R3m$ symmetry) and orthorhombic ($Cmcm$ symmetry) crystal structures, respectively, although both of them are predicted to be either thermodynamically or dynamically unstable. Moreover, recent theoretical calculations indicated that Mg_2N might have a monolayer structure similar to that of Ca_2N, which can generate high harmonics up to 120th order with an efficiency 4 orders of magnitude higher than that of monolayer *h*-BN [5]. Thus, to clarify ambiguities and continue exploring AE_2N as electrides, further investigations on their crystal structures, as well as the associated physicochemical properties, are still highly in demand. Here, starting from the previously reported $R3m$ structure of Be_2N, we derive a crystal structure for both Be_2N and Mg_2N by symmetry analysis, which has a layered framework with $R\bar{3}m$ symmetry. The thermodynamic and dynamic stabilities of this $R\bar{3}m$ structure are first studied and compared to that of all the other structures proposed for AE_2N in the literature. Then, based on the most stable structures obtained, we systematically investigate the electronic and optical properties of Be_2N and Mg_2N as electrode materials.

II. COMPUTATIONAL METHOD

First-principles calculations are performed using the projector augmented wave method [36] with the plane-wave basis set within the DFT framework, as implemented in the Vienna *ab initio* simulation package (VASP) [37,38]. The exchange-correlation energy is treated by the generalized gradient approximation method [39] with the Perdew-Burke-Ernzerhof functional [39], while the Heyd-Scuseria-Ernzerhof (HSE06) hybrid functional [40,41] is adopted to calculate the electronic structures and optical properties. Wave functions are expanded in plane waves up to a kinetic energy cutoff of 550 eV, and Brillouin-zone integrations are performed using the Γ-center *k*-point mesh with a resolution of $2\pi \times 0.03$ $Å^{-1}$. During relaxation, the unit-cell lattice vectors, as well as the atomic coordinates, are fully relaxed until the force on each atom is less than 0.02 eV/Å. To reveal electron localization at the interstitial space in electrides, the charge density around a given atom is integrated based on Bader analysis [42], and the DFT-D3 approach by Grimme is performed to investigate the long-range weak van der Waals interactions [43]. The phonon spectra are calculated by using the frozen-phonon method with a $4 \times 4 \times 1$ supercell, as implemented in the PHONOPY code [44], and ab initio molecular dynamics (AIMD) simulations [45] are performed within a $4 \times 4 \times 1$ supercell by using the constant volume and temperature (NVT ensemble) method, where the temperature is controlled by a Nosé-Hover thermostat.

III. RESULTS AND DISCUSSION

A. Crystal structures of Be_2N and Mg_2N

Like Ca_2N, Be_2N and Mg_2N are important members of the AE_2N family. However, up to now, neither of these materials have been synthesized in experiments and their crystal structures remain unknown. Previous theoretical studies predicted that Be_2N might adopt a rhombohedral structure with $R3m$ symmetry, which is quite different from the structures of Ca_2N, Sr_2N, and Ba_2N [31]. As shown in Fig. 1(a), in this $R3m$ structure, there are two kinds of N atoms: (1) N atoms that are sixfold coordinated with Be atoms to form edge-sharing octahedra, and (2) N atoms that are fivefold coordinated with Be atoms to form corner-sharing hexahedra, both running along the *ab* plane. Each octahedron is then connected to an adjacent hexahedron by sharing one Be atom, so that the stoichiometric $[Be_2N]$ slabs are formed and stacked along the *c* axis in an *ABC* stacking sequence. Excess electrons can be accommodated in the interstitial space (interlayer) between adjacent $[Be_2N]$ slabs, which are supposed to form a 2D anionic electron gas, analogous to Ca_2N. However, DFT calculations indicate that these excess electrons in Be_2N are too localized to interact with each other, and consequently, it is categorized as a 0D electride with semiconducting

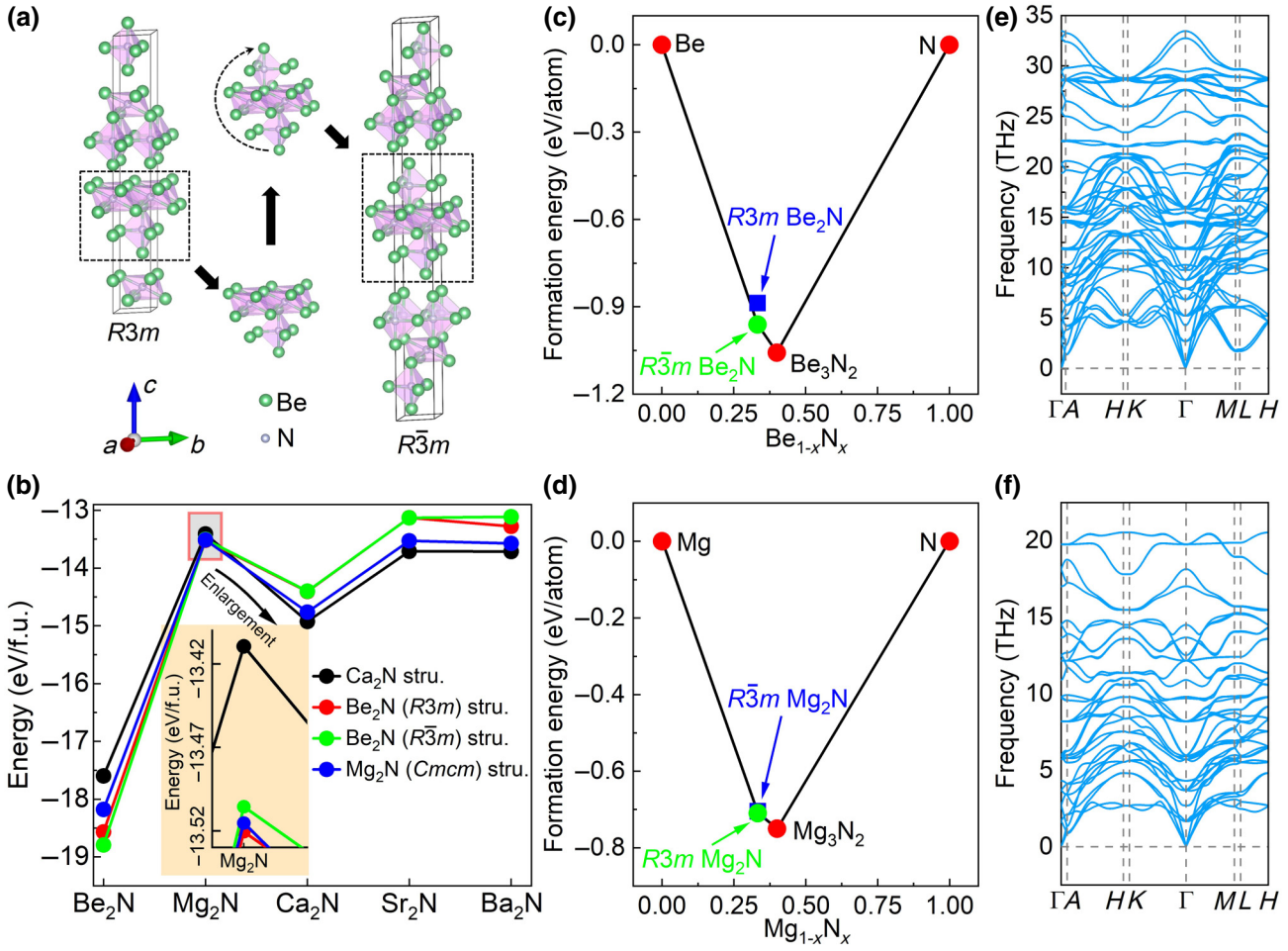

FIG. 1. (a) Derivation from $R3m$ to $R\bar{3}m$ structures of Be_2N. (b) Cohesive energies of AE_2N with different crystal structures (for crystal structures, see Fig. S1 within the Supplemental Material [31,46]). (c),(d) Calculated phase diagrams of Be-N and Mg-N compounds, respectively. (e),(f) Phonon spectra of $R\bar{3}m$ Be_2N and $R3m$ Mg_2N, respectively.

electronic properties [31]. As a typical AE_2N, this result is peculiar, and one may wonder whether there are other structures for Be_2N, such as a 2D electride, which has still not been found.

To answer this question, starting from the $R3m$ structure of Be_2N, we derive crystal structures for both Be_2N and Mg_2N by symmetry analysis. As shown in Fig. 1(a), the original two-sheet-thick [Be_2N] slabs in the $R3m$ structure are converted into three-sheet-thick [Be_2N] slabs in the derived structure by imposing inversion symmetry on the hexahedra sheet next to the octahedra sheet, with their ABC stacking sequence kept unchanged. Since each sheet in [Be_2N] slabs has Be_2N stoichiometry, these symmetry operations will not alter the chemical composition of the entire system. Although, through these operations, the original polar $R3m$ structure is converted into a centrosymmetric structure with $R\bar{3}m$ symmetry, the unit cell of which contains 27 atoms. The lattice constants of this $R\bar{3}m$ structure are calculated to be $a = b = 2.84$ Å and $c = 28.60$ Å, with Be atoms occupying the Wyckoff positions $6c(0.33333, 0.66667, 0.41278)$, $6c(0, 0, 0.19315)$, and $6c(0.66667, 0.33333, 0.69159)$, and N atoms occupying the Wyckoff positions $3b(1, 0, 0.5)$ and $6c(0.66667, 0.33333, 0.74821)$.

To estimate the feasibility of this derived $R\bar{3}m$ structure, we compare its relative stability with other structures proposed in the literature for all AE_2N, as shown in Fig 1(b). For experimentally synthesized compounds, i.e., Ca_2N, Sr_2N, and Ba_2N, the Ca_2N structure is shown to be the most stable, which is consistent with the experimental observations [21,34,35]. For Be_2N, we find that the $R\bar{3}m$ structure becomes the most stable, which has a total energy of 0.025 eV/formula unit (f.u.) lower than that of the previously predicted $R3m$ structure. This may be ascribed to more delocalized anionic electrons in $R\bar{3}m$ Be_2N, compared to that in $R3m$ Be_2N, which could reduce the kinetic energy of the system (see the electronic structure of Be_2N, as discussed below). Moreover, the thermodynamic

stability of $R\bar{3}m$ Be_2N is also considered by calculating its formation energy (E_f) with respect to bulk Be, N_2, and Be_3N_2 which are the only competing compounds on the convex hull of the Be-N system [47], given by

$$E_f = E_{Be_xN_y} - x\mu_{Be} - y\mu_N \quad (1)$$

where $E_{Be_xN_y}$ is the total energy of a given Be_xN_y compound, and μ_{Be} and μ_N are the chemical potentials of Be and N, respectively. The calculated convex hull is shown in Fig. 1(c), which indicates that $R\bar{3}m$ Be_2N is thermodynamically stable. Figure 1(e) shows the calculated phonon spectrum of $R\bar{3}m$ Be_2N. It is clear to see that there are no negative-frequency modes within the entire Brillouin zone, suggesting the dynamic stability of this material. In addition, to take the temperature effect into account, we also perform AIMD simulations on $R\bar{3}m$ Be_2N at 300 and 1000 K, respectively. The results show that the $R\bar{3}m$ structure can withstand above 1000 K and preserve its atomic configuration without any significant distortion [see Fig. S2(a) within the Supplemental Material [46]]. All these DFT calculations thus imply that $R\bar{3}m$ Be_2N might be synthesizable, which calls for further experimental confirmation.

For Mg_2N, on the other hand, previous theoretical predictions show that it may possess an orthorhombic structure with *Cmcm* symmetry, which is, however, dynamically unstable [27]. Here, in contrast, our calculations indicate that the most stable structure of Mg_2N should be the $R3m$ structure, although its energy difference with the *Cmcm* structure is only 0.005 eV/f.u., as shown in Fig. 1(b). More interestingly, different from the *Cmcm* structure, the $R3m$ structure is found to exhibit both thermodynamic and dynamic stabilities, as demonstrated in Figs. 1(d) and 1(f), which implies that it may also be possible to synthesize Mg_2N in this structure.

Moreover, to verify our structure prediction by symmetry analysis, a comprehensive unbiased structure search for Be_2N and Mg_2N is also performed by using CALYPSO code [48,49] (see Fig. S3 within the Supplemental Material [46]). For Be_2N, it is interesting to see that the $R\bar{3}m$ structure is also predicted to be the ground-state structure by CALYPSO calculations, consistent with our symmetry analysis. For Mg_2N, the *Cmcm* structure is predicted to be the ground-state structure, analogous to previous work [27]. However, more accurate DFT calculations indicate that the $R3m$ structure has a lower energy than that of *Cmcm* structure of 0.005 eV/f.u..

B. Electronic structures and physicochemical properties of Be_2N and Mg_2N

With the most stable structures obtained, we next turn to discuss the electronic structures and physicochemical properties of Be_2N and Mg_2N. To understand the electronic properties of $R\bar{3}m$ Be_2N, the electron-localization function (ELF) is first calculated. In general, ELF values close to unity reveal a strong covalent interaction or lone-pair electrons, whereas lower values represent weaker ionic, metallic, or van der Waals interactions. As shown in Fig. 2(a), apart from the localized electrons around N atoms, there is also significant number of electrons distributed in the interstitial space between adjacent $[Be_2N]$ slabs in $R\bar{3}m$ Be_2N, forming a 2D-like electron gas. These excess (anionic) electrons should come from the two Be atoms per Be_2N f.u., which can provide four electrons, and thus, overcompensate for the three electrons required by one N atom. Figure 2(b) shows the band structure of $R\bar{3}m$ Be_2N. It is clear to see that $R\bar{3}m$ Be_2N is a metal, and the metallic states around the Fermi level are dominated by anionic electrons, with only a small hybridization with Be $2s$ and N $2p$ orbitals [see Fig. S4(c) within the Supplemental Material [46]]. This is also reflected by the partial charge-density distribution of these metallic bands, as plotted in Fig. S5 within the Supplemental Material [46]. These characteristic electronic properties imply that $R\bar{3}m$ Be_2N is a 2D electride, like Ca_2N, which is quite different from $R3m$ Be_2N, which is reported to be a 0D electride [31]. More interestingly, we also find that the anionic electrons in $R\bar{3}m$ Be_2N can form a 2D Kagome lattice, as illustrated in Fig. 2(a). It was reported recently that these 2D Kagome anionic electrons might lead to exotic physical properties, such as superconductivity [50].

To stabilize the electride materials, it is generally thought that the size of the interstitial space confining the anionic electrons in their crystal structures should be in the range from 3 to 5 Å [27]. When the size is smaller than this range, electrons would prefer to occupy the conduction bands, while, when the size is larger, electrons tend to escape from the space by thermal excitation [51]. For $R\bar{3}m$ Be_2N, however, we find that this general rule is not obeyed. As shown in Fig. 3(a), the width of the 2D interstitial space in $R\bar{3}m$ Be_2N is only 1.43 Å, which is significantly smaller than the empirical range, while, at the same time, the anionic electrons are still confined in this small space, revealing characteristic 2D electride features. For comparison, we survey the size of interstitial space for several typical electrides, as shown in Fig. 3(b), which all fall into the empirical range of 3–5 Å. To understand this anomalous feature of $R\bar{3}m$ Be_2N, we further inspect its anionic electrons. It is well known that, in electrides, the anionic electrons located in their structural cavities behave like anions, which form bonds with surrounding cations, just like the intermetallic bonds formed in metals [e.g., the hybridization between anionic electrons (X states) and Be $2s$ states in Fig. 2(b) suggests the formation of Be—Be intermetallic bonds in Be_2N]. Thus, the greater the number of anionic electrons confined, the stronger the intermetallic bonds formed, which, in turn, lead to a smaller interstitial space. Figure 3(c) shows the calculated Bader charge of anionic electrons in $R\bar{3}m$ Be_2N. When the c axis is not stretched,

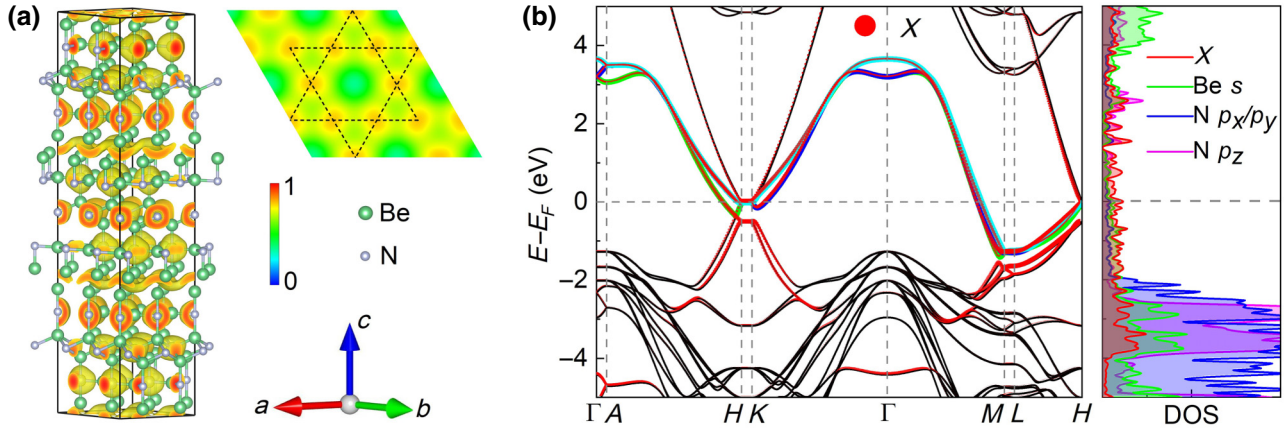

FIG. 2. (a) 3D ELF for $R\bar{3}m$ Be_2N with isosurface = 0.7, and 2D maps are plotted with a 2×2 supercell for the top (001) plane. (b) Band structure and projected density of states (PDOS) of $R\bar{3}m$ Be_2N. Contribution of interstitial anionic electrons [labeled as X in Fig. S4(a) within the Supplemental Material [46]] is highlighted in red. Three bands passing the Fermi surface colored with green, blue, and cyan, and corresponding 3D partial charge densities at a value of 0.003 e/Å^3 are displayed in Figs. S5(a)–S5(c) within the Supplemental Material [46], respectively.

we find there are -0.13 $|e|$ confined in each interlayer between adjacent $[Be_2N]$ slabs (denoted as $[Be_2N]^{0.13+} \cdot 0.13e^-$) in $R\bar{3}m$ Be_2N, which is significantly larger than the anionic electrons confined between the $[Ca_2N]$ slabs in Ca_2N ($[Ca_2N]^{0.038+} \cdot 0.038e^-$). These results indicate that the Be—Be intermetallic bonds formed in $R\bar{3}m$ Be_2N are much stronger than the Ca—Ca intermetallic bonds formed in Ca_2N, which result in the anomalously small interstitial space in $R\bar{3}m$ Be_2N.

Experimentally, the interstitial space in 2D electrides can be modulated by several methods during the synthesis process, such as by inserting h-BN buffer layers [52] or by imposing nanomechanical pressure [53]. Here, we also investigate how the mechanical strain will influence the anionic electrons in $R\bar{3}m$ Be_2N, as shown in Fig. 3(c). As the structure of $R\bar{3}m$ Be_2N is continuously stretched along the c axis, we find that the number of anionic electrons decreases gradually from -0.13 to -0.07 $|e|$ per f.u. (until the stretching strain reaches a maximum of 21%), indicating that the electrons are transferred from the interstitial space to the cationic framework. Moreover, within $[Be_2N]$ slabs, we find that the N_1 atoms gain electrons, while the N_2 atoms lose electrons in nearly the same amount, which tends to cancel each other out, and the charge around the Be_1 and Be_2 atoms remains almost unchanged. Thus, the anionic electrons should be mainly transferred to the Be_3 atoms, with their Bader charges changing from 0.75 to 0.63 $|e|$, indicating that each Be_3 atom gains -0.12 $|e|$ at 21% stretching strain. Continuing to stretch the structure leads to the cleavage of $R\bar{3}m$ Be_2N at an energy cost of 4.81 J/m^2, as illustrated in Fig. 3(d). This cleavage energy is significantly larger than that for Ca_2N (1.09 J/m^2) [54]. Moreover, bond breaking does not occur at the interstitial space but within $[Be_2N]$ slabs, which also demonstrates the strong bonding effect between the anionic electrons and cationic $[Be_2N]$ slabs in $R\bar{3}m$ Be_2N (the Be—Be intermetallic bonds).

The small interstitial space in $R\bar{3}m$ Be_2N also leads to other anomalous physical properties. For electrides, the work function (W_F) is typically low, because of the loosely bound anionic electrons. However, this is not the case for $R\bar{3}m$ Be_2N, as discussed above. As a consequence, the W_F of $R\bar{3}m$ Be_2N is calculated to be 3.76 eV, as shown in Fig. 3(e), which is higher than that found for other electride materials (less than 3.5 eV [21,23,55–58], see Table S1 within the Supplemental Material [46]). This implies a relatively hard electron extraction from $R\bar{3}m$ Be_2N. Figure 4 shows the optical absorption coefficient and plasma frequency (ω_p) of $R\bar{3}m$ Be_2N. Interestingly, a large anisotropy in the optical absorptions is observed. As shown in Fig. 4(a), there are significant optical absorptions in the entire energy window (from 0 to 6 eV) along the x and y directions. On the other hand, the absorptions in the z direction are relatively low below 3.5 eV, with a small plasma frequency of 0.65 eV/$\hbar$. These results imply that $R\bar{3}m$ Be_2N will be opaque in the x and y directions, but quite transparent in the z direction for visible light. Indeed, the simulated optical transmission spectra about the z direction for a free-standing 100-nm-thick slab shows that the sample has an average of 60% transmittance for visible light, suggesting that $R\bar{3}m$ Be_2N may be used as a privacy-film material [59].

Compared to $R\bar{3}m$ Be_2N, the electronic structures and physicochemical properties of $R3m$ Mg_2N are quite different. Figures 5(a) and 5(b) show the calculated ELF and band structure of $R3m$ Mg_2N. It is clear to see that $R3m$ Mg_2N is a 0D electride with a semiconducting band structure. This is because the anionic electrons in $R3m$

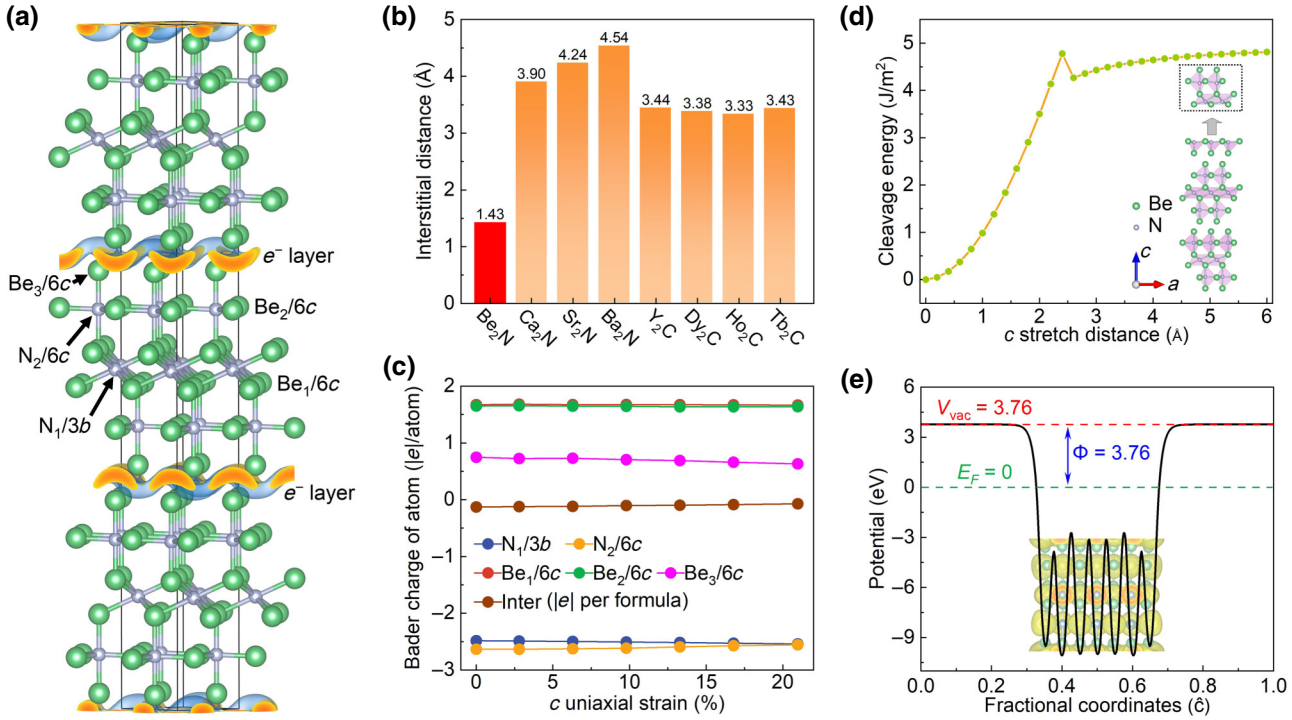

FIG. 3. (a) Interstitial layer positions and Wyckoff sites of nonequivalent atoms in $R\bar{3}m$ Be_2N. (b) Interstitial distances of several typical electrides. (c) Bader charge of Be, N, and X atoms as a function of c-axis stretching strain. (d) Cleavage energy as a function of the stretching distance along the c axis in $R\bar{3}m$ Be_2N. (e) Work functions of $R\bar{3}m$ Be_2N for the (110) surface.

Mg_2N are well confined in individual structural cavities, and thus, cannot efficiently interact with each other to form itinerate bands. As a result, an indirect band gap of 0.22 eV (based on HSE06 calculations) appears with the band edges located near the A and H points. The calculated PDOS indicate that the valence-band maximum states are predominately contributed to by the anionic electrons, while the conduction-band minimum states are constructed by the hybridization between Mg $3s$ and N $2p_z$ orbitals (see Fig. S6 within the Supplemental Material [46]). Bader analysis shows that there are -0.45 $|e|$/f.u. located in the structural cavities in $R3m$ Mg_2N, which is much larger than that in $R\bar{3}m$ Be_2N.

The width of interstitial space is found to be 2.42 Å in $R3m$ Mg_2N, which is larger than that in $R\bar{3}m$ Be_2N, but still outside the empirical range. As shown in Fig. 5(d), the W_F of $R3m$ Mg_2N is calculated to be 3.21 eV, which is smaller than that of $R\bar{3}m$ Be_2N. The above results imply

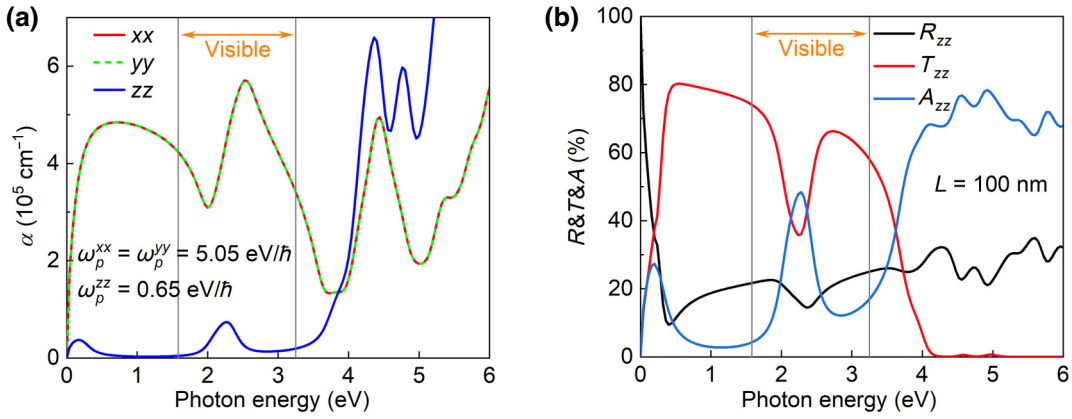

FIG. 4. Optical properties of $R\bar{3}m$ Be_2N. (a) Calculated absorption coefficients with plasma frequencies of $\omega_p^{xx} = \omega_p^{yy} = 5.05$ eV/$\hbar$ and $\omega_p^{zz} = 0.65$ eV/$\hbar$. (b) Reflection (R_{zz}), transmission (T_{zz}), and absorption (A_{zz}) spectra for a 100-nm-thick Be_2N slab with optically smooth surfaces.

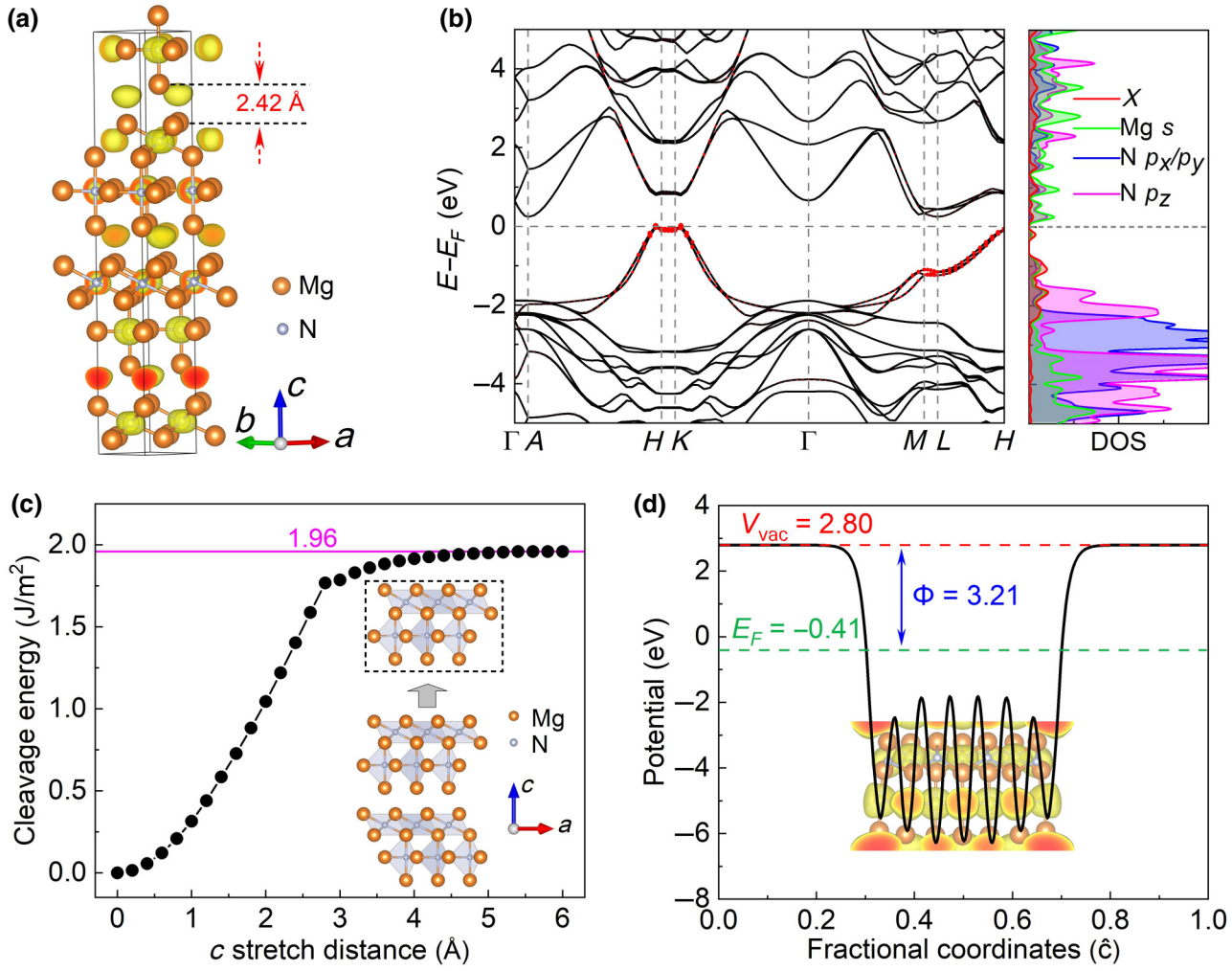

FIG. 5. (a) ELF of $R3m$ Mg_2N with isosurface = 0.75. (b) Band structure and PDOS of $R3m$ Mg_2N, with the contribution of interstitial anionic electrons (labeled as X) highlighted in red. (c) Cleavage energy as a function of stretching distance along the c axis in $R3m$ Mg_2N. (d) Work functions of $R3m$ Mg_2N along the [110] directions.

that the interaction of anionic electrons with surrounding cations in $R3m$ Mg_2N is smaller than that in $R\bar{3}m$ Be_2N, which may be ascribed to their localized nature. As a consequence, the cleavage energy of $R3m$ Mg_2N is calculated to be 1.96 J/m^2, as shown in Fig. 5(c), which is comparable to that of Ca_2N. This result suggests that the exfoliation of Mg_2N into monolayers would be energetically possible, which was recently proposed as a high-harmonic generator based on time-dependent DFT calculations [5].

IV. CONCLUSION

By structure and symmetry analysis, we show that Be_2N possesses a ground-state structure with $R\bar{3}m$ symmetry, which is more stable than the previously predicted $R3m$ structure, with an energy difference of 0.025 eV/f.u. Moreover, different from $R3m$ Be_2N, which is predicted to be a 0D electride, $R\bar{3}m$ Be_2N is demonstrated to be a 2D electride with excess electrons located in the interstitial space forming a 2D Kagome lattice. Furthermore, compared to other 2D electrides, $R\bar{3}m$ Be_2N shows anomalous physicochemical properties, such as having a small interstitial space of 1.43 Å, a high work function of 3.76 eV, and a large cleavage energy of 4.81 J/m^2, which can be ascribed to the relatively strong bonding effect between the anionic electrons and cationic framework. For Mg_2N, on the other hand, we find that the $R3m$ structure is the most stable, with a total energy of 0.015 and 0.005 eV/f.u. lower than that of $R\bar{3}m$ and $Cmcm$ structures, respectively. Moreover, different from $R\bar{3}m$ Be_2N, $R3m$ Mg_2N is shown to be a 0D electride, exhibiting a semiconducting band structure with an indirect band gap of 0.22 eV. The interstitial space of $R3m$ Mg_2N is larger than that of $R\bar{3}m$ Be_2N, but the work functions and cleavage energy of $R3m$ Mg_2N are smaller than that of $R\bar{3}m$ Be_2N, mainly due to the reduced interaction of their anionic electrons with surrounding cations.

The exotic physicochemical properties of Be_2N and Mg_2N may lead to various potential applications. For instance, like Ca_2N, the high mobility of 2D electron gas in $R\bar{3}m$ Be_2N could make it a platform for exploring topological materials. Moreover, different from Ca_2N, the 2D electron gas in $R\bar{3}m$ Be_2N forms a 2D Kagome lattice. It was reported recently that this 2D Kagome electronic band could lead to special physical properties, such as low-temperature superconductivity [3,50]. Furthermore, as discussed above, $R\bar{3}m$ Be_2N has quite distinct optical absorption coefficients along different crystalline directions, which thus may be used as privacy-film materials [55]. For Mg_2N, on the other hand, our calculations indicate that exfoliation of its bulk material into monolayers is energetically possible. As predicted by time-dependent DFT calculations, the Mg_2N monolayer can be used as a high-harmonic generator, which can generate high harmonics up to 120th order with an efficiency 4 orders of magnitude higher than that of the *h*-BN monolayer [5]. In addition, close contact of the Mg_2N monolayer with other 2D materials by van der Waals epitaxy would create special electronic states, such as heavy electron doping into hard-doping 2D materials.

ACKNOWLEDGMENTS

This work is supported by the Guangdong Basic and Applied Basic Research Foundation (Grant No. 2021A1515010219), the Shenzhen Science and Technology Program (Grant No. KQTD20180412181422399), High-Level University Construction Funds of SZU (Grant No. 866-000002110709), the Natural Science Foundation of Guangdong Province (Grant No. 2022A1515011990), the National Key R&D Program of China (Grant No. 2019YFB2204500), the Science and Technology Innovation Commission of Shenzhen (Grant No. JCYJ20180507181858539), and the National Natural Science Foundation of China (Grants No. 11991060, No. 12088101, and No. U1930402).

The authors declare no competing interest.

[1] J. S. Landers, J. L. Dye, A. Stacy, and M. J. Sienko, Temperature-dependent electron spin interactions in lithium [2.1.1] cryptate electride powders and films, J. Phys. Chem. **85**, 1096 (1981).

[2] M. Miyakawa, S. W. Kim, M. Hirano, Y. Kohama, H. Kawaji, T. Atake, H. Ikegami, K. Kono, and H. Hosono, Superconductivity in an inorganic electride $12CaO \cdot 7Al_2O_3 : e^-$, J. Am. Chem. Soc. **129**, 7270 (2007).

[3] X. Qiu, J. Zhang, H. Yang, Z. Lu, and K. Liu, Superconductivity in monolayer Ba_2N electride: First-principles study, Phys. Rev. B **105**, 165101 (2022).

[4] H. Hosono, Exploring electro-active functionality of transparent oxide materials, Jpn. J. Appl. Phys. **52**, 90001 (2013).

[5] J. K. An, K. H. Kim, and M. I. Choe, High-harmonic generation from 2D monolayer electrides, Ann. Phys. **534**, 2100368 (2022).

[6] S. Y. Lee, J. Hwang, J. Park, C. N. Nandadasa, Y. Kim, J. Bang, K. Lee, K. H. Lee, Y. Zhang, Y. Ma, *et al.*, Ferromagnetic quasi-atomic electrons in two-dimensional electride, Nat. Commun. **11**, 1526 (2020).

[7] J. Hu, B. Xu, S. A. Yang, S. Guan, C. Ouyang, and Y. Yao, 2D electrides as promising anode materials for Na-ion batteries from first-principles study, ACS Appl. Mater. Interfaces **7**, 24016 (2015).

[8] S. Watanabe, T. Watanabe, K. Ito, N. Miyakawa, S. Ito, H. Hosono, and S. Mikoshiba, Secondary electron emission and glow discharge properties of $12CaO \cdot 7Al_2O_3$ electride for fluorescent lamp applications, Sci. Technol. Adv. Mater. **12**, 34410 (2011).

[9] Y. Gong, H. Li, C. Li, X. Yang, J. Wang, and H. Hosono, LaRuSi electride disrupts the scaling relations for ammonia synthesis, Chem. Mater. **34**, 1677 (2022).

[10] Y. Toda, H. Hirayama, N. Kuganathan, A. Torrisi, P. V. Sushko, and H. Hosono, Activation and splitting of carbon dioxide on the surface of an inorganic electride material, Nat. Commun. **4**, 2378 (2013).

[11] L. D. Le, D. Issa, B. Van Eck, and J. L. Dye, Preparation of alkalide and electride films by direct vapor deposition, J. Phys. Chem. **86**, 7 (1982).

[12] D. J. Singh, H. Krakauer, C. Haas, and W. E. Pickett, Theoretical determination that electrons act as anions in the electride $Cs^+(15\text{-crown-}5)_2 \cdot e^-$, Nature **365**, 39 (1993).

[13] A. Ellaboudy, J. L. Dye, and P. B. Smith, Cesium 18-crown-6 compounds. A crystalline ceside and a crystalline electride, J. Am. Chem. Soc. **105**, 6490 (1983).

[14] M. J. Wagner, R. H. Huang, J. L. Eglin, and J. L. Dye, An electride with a large six-electron ring, Nature **368**, 726 (1994).

[15] R. H. Huang, M. J. Wagner, D. J. Gilbert, K. A. Reidy-Cedergren, D. L. Ward, M. K. Faber, and J. L. Dye, Structure and properties of $Li^+(\text{cryptand}[2.1.1])e^-$, an electride with a 1D "spin-ladder-like" cavity-channel geometry, J. Am. Chem. Soc. **119**, 3765 (1997).

[16] M. Y. Redko, J. E. Jackson, R. H. Huang, and J. L. Dye, Design and synthesis of a thermally stable organic electride, J. Am. Chem. Soc. **127**, 12416 (2005).

[17] A. A. Dyachenko, A. V. Lukoyanov, V. I. Anisimov, and A. R. Oganov, Electride properties of ternary silicide and germanide of La and Ce, Phys. Rev. B **105**, 85146 (2022).

[18] S. Matsuishi, Y. Toda, M. Miyakawa, K. Hayashi, T. Kamiya, M. Hirano, I. Tanaka, and H. Hosono, High-density electron anions in a nanoporous single crystal: $[Ca_{24}Al_{28}O_{64}]^{4+}(4e^-)$, Science **301**, 626 (2003).

[19] K. Kim, M. Kikuchi, M. Miyakawa, H. Yanagi, T. Kamiya, M. Hirano, and H. Hosono, Photoelectron spectroscopic study of C12A7 : e^- and Alq3 interface: The formation of a low electron-injection barrier, J. Phys. Chem. C **111**, 8403 (2007).

[20] M. Kitano, Y. Inoue, Y. Yamazaki, F. Hayashi, S. Kanbara, S. Matsuishi, T. Yokoyama, S. Kim, M. Hara, and H. Hosono, Ammonia synthesis using a stable electride as an electron donor and reversible hydrogen store, Nat. Chem. **4**, 934 (2012).

[21] K. Lee, S. W. Kim, Y. Toda, S. Matsuishi, and H. Hosono, Dicalcium nitride as a two-dimensional electride with an anionic electron layer, Nature **494**, 336 (2013).

[22] J. Wu, J. Li, Y. Gong, M. Kitano, T. Inoshita, and H. Hosono, Intermetallic electride catalyst as a platform for ammonia synthesis, Angew. Chem., Int. Ed. **58**, 825 (2019).

[23] J. Wang, K. Hanzawa, H. Hiramatsu, J. Kim, N. Umezawa, K. Iwanaka, T. Tada, and H. Hosono, Exploration of stable strontium phosphide-based electrides: Theoretical structure prediction and experimental validation, J. Am. Chem. Soc. **139**, 15668 (2017).

[24] S. H. Kang, D. Thapa, B. Regmi, S. Ren, Y. Kim, S. Kim, and S. W. Kim, Chemically stable low-dimensional electrides in transition metal-rich monochalcogenides: Theoretical and experimental explorations, J. Am. Chem. Soc. **144**, 4496 (2022).

[25] S. H. Kang, J. Bang, K. Chung, C. N. Nandadasa, G. Han, S. Lee, K. H. Lee, K. Lee, Y. Ma, S. H. Oh, *et al.*, Water- and acid-stable self-passivated dihafnium sulfide electride and its persistent electrocatalytic reaction, Sci. Adv. **6**, a7416 (2020).

[26] T. Tada, S. Takemoto, S. Matsuishi, and H. Hosono, High-throughput *ab initio* screening for two-dimensional electride materials, Inorg. Chem. **53**, 10347 (2014).

[27] T. Inoshita, S. Jeong, N. Hamada, and H. Hosono, Exploration for Two-Dimensional Electrides via Database Screening and *Ab Initio* Calculation, Phys. Rev. X **4**, 31023 (2014).

[28] L. A. Burton, F. Ricci, W. Chen, G. Rignanese, and G. Hautier, High-throughput identification of electrides from all known inorganic materials, Chem. Mater. **30**, 7521 (2018).

[29] Q. Zhu, T. Frolov, and K. Choudhary, Computational discovery of inorganic electrides from an automated screening, Matter **1**, 1293 (2019).

[30] J. Zhou, L. Shen, M. Yang, H. Cheng, W. Kong, and Y. P. Feng, Discovery of hidden classes of layered electrides by extensive high-throughput material screening, Chem. Mater. **31**, 1860 (2019).

[31] Y. Zhang, H. Wang, Y. Wang, L. Zhang, and Y. Ma, Computer-Assisted Inverse Design of Inorganic Electrides, Phys. Rev. X **7**, 11017 (2017).

[32] S. Kanno, T. Tada, T. Utsumi, K. Nakamura, and H. Hosono, Electronic correlation strength of inorganic electrides from first principles, J. Phys. Chem. Lett. **12**, 12020 (2021).

[33] W. Li, Y. You, and J. Choi, Oxidation, stability, and magnetic ground states of two-dimensional layered electrides, J. Phys. Chem. C **124**, 25316 (2020).

[34] N. E. Brese and M. O'Keeffe, Synthesis, crystal structure, and physical properties of Sr_2N, J. Solid State Chem. **87**, 134 (1990).

[35] E. T. Keve and A. C. Skapski, Crystal structure of dicalcium nitride, Inorg. Chem. **7**, 1757 (1968).

[36] P. E. Blöchl, Projector augmented-wave method, Phys. Rev. B **50**, 17953 (1994).

[37] G. Kresse and J. Furthmüller, Efficiency of *ab-initio* total energy calculations for metals and semiconductors using a plane-wave basis set, Comput. Mater. Sci. **6**, 15 (1996).

[38] G. Kresse and D. Joubert, From ultrasoft pseudopotentials to the projector augmented-wave method, Phys. Rev. B **59**, 1758 (1999).

[39] J. P. Perdew, K. Burke, and M. Ernzerhof, Generalized Gradient Approximation Made Simple, Phys. Rev. Lett. **77**, 3865 (1996).

[40] J. Heyd, G. E. Scuseria, and M. Ernzerhof, Hybrid functionals based on a screened Coulomb potential, J. Chem. Phys. **118**, 8207 (2003).

[41] J. Paier, M. Marsman, K. Hummer, G. Kresse, I. C. Gerber, and J. G. Ángyán, Screened hybrid density functionals applied to solids, J. Chem. Phys. **124**, 154709 (2006).

[42] W. Tang, E. Sanville, and G. Henkelman, A grid-based Bader analysis algorithm without lattice bias, J. Phys.: Condens. Matter **21**, 84204 (2009).

[43] S. Grimme, J. Antony, S. Ehrlich, and H. Krieg, A consistent and accurate *ab initio* parametrization of density functional dispersion correction (DFT-D) for the 94 elements H-Pu, J. Chem. Phys. **132**, 154104 (2010).

[44] A. Togo, F. Oba, and I. Tanaka, First-principles calculations of the ferroelastic transition between rutile-type and $CaCl_2$-typeSiO_2 at high pressures, Phys. Rev. B **78**, 134106 (2008).

[45] G. J. Martyna, M. L. Klein, and M. Tuckerman, Nosé-Hoover chains: The canonical ensemble via continuous dynamics, J. Chem. Phys. **97**, 2635 (1992).

[46] See the Supplemental Material at http://link.aps.org/supplemental/10.1103/PhysRevApplied.19.034014 for crystal structures, AIMD simulation, CALYPSO predictions, and projected band structures of $R\bar{3}m$ Be_2N and $R3m$ Mg_2N.

[47] A. Jain, S. P. Ong, G. Hautier, W. Chen, W. D. Richards, S. Dacek, S. Cholia, D. Gunter, D. Skinner, G. Ceder, and K. A. Persson, Commentary: The materials project: A materials genome approach to accelerating materials innovation, APL Mater. **1**, 11002 (2013).

[48] Y. Wang, J. Lv, L. Zhu, and Y. Ma, Crystal structure prediction via particle-swarm optimization, Phys. Rev. B **82**, 094116 (2010).

[49] Y. Wang, J. Lv, L. Zhu, and Y. Ma, CALYPSO: A method for crystal structure prediction, Comput. Phys. Commun. **183**, 2063 (2012).

[50] J. You, B. Gu, G. Su, and Y. P. Feng, Emergent Kagome electrides, J. Am. Chem. Soc. **144**, 5527 (2022).

[51] H. Hosono and M. Kitano, Advances in materials and applications of inorganic electrides, Chem. Rev. **121**, 3121 (2021).

[52] H. Fang, C. Battaglia, C. Carraro, S. Nemsak, B. Ozdol, J. S. Kang, H. A. Bechtel, S. B. Desai, F. Kronast, A. A. Unal, *et al.*, Strong interlayer coupling in van der Waals heterostructures built from single-layer chalcogenides, Proc. Natl. Acad. Sci. U. S. A. **111**, 6198 (2014).

[53] G. S. Verhoeven, N. Pradeep, J. W. M. Frenken, J. A. Heimberg, H. W. Zandbergen, and M. Dienwiebel, Superlubricity of Graphite, Phys. Rev. Lett. **92**, 126101 (2004).

[54] S. Zhao, Z. Li, and J. Yang, Obtaining two-dimensional electron gas in free space without resorting to electron doping: An electride based design, J. Am. Chem. Soc. **136**, 13313 (2014).

[55] Y. Toda, H. Yanagi, E. Ikenaga, J. J. Kim, M. Kobata, S. Ueda, T. Kamiya, M. Hirano, K. Kobayashi, and H.

Hosono, Work function of a room-temperature, stable electride $[Ca_{24}Al_{28}O_{64}]^{4+}(e^-)_4$, Adv. Mater. **19**, 3564 (2007).

[56] K. Li, Y. Gong, J. Wang, and H. Hosono, Electron-deficient-type electride Ca_5Pb_3: Extension of electride chemical space, J. Am. Chem. Soc. **143**, 8821 (2021).

[57] C. Wang, M. Xu, K. T. Butler, and L. A. Burton, Ultralow work function of the electride Sr_3CrN_3, Phys. Chem. Chem. Phys. **24**, 8854 (2022).

[58] Y. Lu, J. Li, T. Tada, Y. Toda, S. Ueda, T. Yokoyama, M. Kitano, and H. Hosono, Water durable electride Y_5Si_3: Electronic structure and catalytic activity for ammonia synthesis, J. Am. Chem. Soc. **138**, 3970 (2016).

[59] J. Kim, C. H. Lee, S. S. Lee, and K. Lee, Highly transparent privacy filter film with image distortion, Opt. Express **22**, 29799 (2014).